Modelling and simulation of reactive transport phenomena

Adoliwine E. Amikiya and Mapundi K. Banda

Department of Mathematics and Applied Mathematics, Botany Building, University of Pretoria, Hatfield 0028, South Africa.
E-mail: amixaddsmall@yahoo.com

Applied Mathematics, Stellenbosch University, Private Bag X1, Matieland 7602, South Africa

Abstract

Mathematical modelling and numerical simulation of chemical transport phenomena are very challenging due to large numbers of species and reactions involved. Reactive transport models for such systems have high degrees of freedom, and therefore, are computationally expensive to solve. In this discussion, we present and numerically analyse stoichiometric decoupling method for reducing the high degrees of freedom and hence, cost of simulation. This method is a model reduction procedure that is based on some key properties of chemical systems. A multi-scale model of a passive treatment method for acidic mine effluents is used to test the efficacy of the reduction procedure. Moreover, reduced models are characteristically non-linear and stiff, thus, we used numerical techniques to study the reduction error in order to establish compatibility/efficiency of the reduction procedure.

Keywords: Modelling, simulation, chemical transport, model reduction, nonlinear, numerical techniques.

2000 MSC: 92E20, 80A30, 92F05

1. Introduction

Multi-scale modelling of reactive transport phenomena can enhance our understanding of chemical processes and also provide useful quantitative information for policy-making and for improving engineering designs.

However, due to the presence of many chemical species in most chemical systems, multi-scale models for reactive transport phenomena usually have high degrees of freedom and therefore, are computationally expensive to analyse or solve. Thus, it is necessary for model reduction techniques to be developed for such systems. Model reduction techniques have been developed and applied to many biochemical systems that do not involve transport phenomena. The reduction techniques and resulting approximations are in general, based on a partial equilibrium assumption, a quasi steady state assumption and a computational singular perturbation analysis of the system of interest [1, 2, 3].

Quasi steady state approximations (QSSAs) are common reduction techniques that have been successfully applied in biochemical systems for many years [1, 4]. The QSSAs reduce large systems by replacing derivatives of some species (in the system which are assumed to be in quasi equilibrium) with algebraic functions. However, it is reported

in [3, 5, 6, 7], that QSSAs lose some relevant properties of their original systems, and therefore, cannot be applied in some frameworks (e. g. reactive transport modelling where accuracy is a key issue).

Partial equilibrium approximations (PEA) form another class of reduction methods that have also been extensively applied in biochemical systems [1, 4]. The PEA sets derivatives corresponding to fast reactions, to zero, thus only derivatives corresponding to slow reactions are considered in dynamical studies of the system [1, 2, 8]. The disadvantage is that, the fast reactions of the system must be known in advance [1, 2]. This class is also not the best reduction method in reactive transport processes where accuracy is a key issue and information on fast reactions is usually not available.

Computational singular perturbation (CSP) methods are not extensively applied in chemical kinetics. The CSP decouples the ordinary differential equations corresponding to the species rate profiles into linearly independent modes, which can then be classified into fast and slow groups. It is based on eigen-decomposition of the original system [3]. This method can be applied in reactive transport processes, however, basis functions are required in the eigen-decomposition process of decoupling the original system. Finding such basis functions is not an obvious task [3].

Stoichiometry and species mass balances are two internal properties of chemical systems that can be coupled and applied to uncouple a system of equations that represent rate profiles for the species in the system. This method is most appropriate when some of the many species are of interest. In this discussion, we present and numerically analyse this stoichiometric reduction procedure. The behaviour of the reduction error with respect to high, low or normal Peclet numbers will be analysed using numerical schemes, in order to establish efficiency and compatibility of the decoupling procedure.

Furthermore, one economically feasible class of acidic effluent treatment methods is passive treatment methods, which encompasses all simple and less expensive pH raising and metal removal techniques that make use of natural energy sources (e.g. gravity, microbial metabolic energy, photosynthesis)[9, 10]. The commonest pH raising technique involves the use of limestone or lime [11, 12, 13]. A physico-chemical process takes place leading to reduction in the contaminant concentration. The idea of treatment is to convert some of the water contaminants (that are usually toxic, corrosive and environmentally unfriendly) to stable and environmentally friendly forms. Thus one only needs to keep track of the temporal and spatial distributions corresponding to such species. Therefore, for validation and verification of the procedure, we use a multi-scale model that describes reactive transport processes in the passive treatment of acidic mine effluent water.

There are four Sections in this discussion. Section 1, contains the introduction to our study and a brief review of literature on model reduction. In Section 2, we build a mathematical model (with six degrees of freedom) based on experimentally obtained kinetic data for physico-chemical processes that occur in the passive treatment of acidic mine effluent water, and then reduce the six degrees of freedom to three (using stoichiometry and mass balance techniques). In Section 3, we present a backward (implicit) Euler time scheme with three spatial numerical schemes that each perform best in one of three flow regimes (high, low or normal Peclet number regimes). The schemes are also verified and applied to solve both multi-scale models (large and reduced models) in Section 3. We finally conclude the discussion in Section 4.

2. Reactive transport models

Multi-scale physico-chemical processes of reactive transport phenomena in porous domains can be described by the following generalized hydro-geochemical fluid flow model (see [14, 15, 16] for detailed discussions on fluid flow through porous media):

$$\nabla \cdot \mathbf{v} = 0, \tag{1}$$

$$\varepsilon_f \nabla p = \varepsilon_f \rho \mathbf{g} - K_h \mathbf{v}, \tag{2}$$

$$\frac{\partial \varepsilon_f U_k}{\partial t} + \nabla \cdot \Big(\varepsilon_f \mathbf{v} U_k\Big) - \nabla \cdot \Big(\varepsilon_f \mathbf{D} \cdot \nabla U_k\Big) = S_k, \tag{3}$$

where U_k is the mass concentration of the k^{th} species, $\mathbf{D}$ is a tensor for dispersivities, S_k is a source or sink for the k^{th} species, $\mathbf{v}$ is the seepage velocity vector, ρ is density of effluent water, p is pressure, t is time, μ is viscosity of effluent water, ε_f is porosity of the flow domain, ∇ is a spatial derivative vector, $\mathbf{g}$ is gravitational force per unit mass, $K_h = \frac{\mu}{K_p}$ is the hydraulic conductivity and K_p is permeability of the porous medium.

Equations (1)-(2) are the continuity and momentum equations for the fluid flow, respectively, and Equation (3) is the species transport and reaction equation.

Closure of the transport Equation (3) requires kinetic data from the chemical system under consideration. Let $N_{f,r}$ and $N_{b,r}$ be total species numbers in the forward and backward reactions of an r^{th} elementary reaction, respectively. The mechanism for a system of M elementary reactions involving N chemical species is generally written as:

$$\sum_{i=1}^{N_{f,r}} a_{r,i} A_{r,i} \rightleftharpoons \sum_{j=1}^{N_{b,r}} b_{r,j} B_{r,j}, \quad r = 1, \ldots, M, \tag{4}$$

where $a_{r,i}$ and $b_{r,j}$ are stoichiometric coefficients for the species $A_{r,i}$ and $B_{r,j}$ in the r^{th} elementary reaction. In general, $\sum_{r=1}^{M}(N_{f,r} + N_{b,r}) \neq N$ due to the presence of networking species (i.e species engaged in more than one elementary reaction).

Further, denote $\mathbf{C}$ and $\mathbf{U}$ as vectors of all species and their concentrations, respectively. Let a subset of the above species participating in an r^{th} elementary reaction with $N_{f,r}$ and $N_{b,r}$ being the total number of species participating in the reactions on the left and right side, respectively, be denoted as:

$$\begin{aligned} \mathbf{C}_r &= (A_{r,1}, A_{r,2}, \ldots A_{r,N_{f,r}}, B_{r,1}, B_{r,2}, \ldots B_{r,N_{b,r}}) \\ &= (C_{r,1}, C_{r,2}, \ldots C_{r,N_{f,r}}, C_{r,N_{f,r+1}}, C_{r,N_{f,r+2}}, \ldots C_{r,N_r}) \end{aligned}$$

where $N_r = N_{f,r} + N_{b,r}$. Similarly, let

$$\begin{aligned} \mathbf{U}_r &= ([A]_{r,1}, [A]_{r,2}, \ldots [A]_{r,N_{f,r}}, [B]_{r,1}, [B]_{r,2}, \ldots [B]_{r,N_{b,r}}), \\ &= (U_{r,1}, U_{r,2}, \ldots U_{r,N_{f,r}}, U_{r,N_{f,r+1}}, U_{r,N_{f,r+2}}, \ldots U_{r,N_r}) \end{aligned}$$

for $r = 1, 2, \ldots, M$. Further, we define

$$\alpha_r = (\alpha_{r,1}, \alpha_{r,2}, \ldots, \alpha_{N_r})$$

as the respective orders of the species in $\mathbf{C}_r$ and

$$\sigma_r = (\sigma_{r,1}, \sigma_{r,2}, \ldots, \sigma_{r,N_r})$$

as their respective stoichiometric coefficients.

The rate at which the r^{th} elementary reaction (4) proceeds can in general, be expressed as follows:

$$R_r(\mathbf{U}) = K_{fr} \prod_{i=1}^{N_{f,r}} U_{r,i}^{\alpha_{r,i}} - K_{b,r} \prod_{j=N_{f,r}+1}^{N_r} U_{r,j}^{\alpha_{r,j}}, \; r = 1, \ldots, M \tag{5}$$

where $K_{f,r}$, $K_{b,r}$ are the forward and backward reaction constants. From Equation (5), we obtain the rate at which the k^{th} species evolves as:

$$\begin{aligned} S_k &= \sum_{r=1}^{M} \sigma_{rk} R_r, \\ &= \sum_{r=1}^{M} \sigma_{rk} \Big(K_{fr} \prod_{i=1}^{N_{f,r}} U_{r,i}^{\alpha_{r,i}} - K_{b,r} \prod_{j=N_{f,r}+1}^{N_r} U_{r,j}^{\alpha_{r,j}} \Big), \; k = 1, \ldots, N, \end{aligned} \tag{6}$$

Observe that the source/sink term $S_k(U_1, \ldots, U_k, \ldots, U_N)$ defined in Equation (6), is a polynomial in N variables (i.e. concentrations of all the species). Therefore, to solve (3) for the unknown U_k, requires U_i, for $i \neq k$. However, mechanisms are usually very large (i.e. M is large) and contain many species (N is large). Thus, the source/sink terms (6) are expensive to compute. In many experimental and modelling studies, very few of the species are of interest to the researcher, however, due to networking with other species, the species of interest can not be treated in isolation without first decoupling. In Sections 3, we present a decoupling procedure that significantly reduces computational cost by replacing the N variable polynomial (6) by a one-variable polynomial.

2.1. Stoichiometric decoupling method

Denote the initial concentration by $\mathbf{U}_0$, $\mathbf{U}_S$ the concentration due to some source/sink, $\mathbf{U}_T$ the transformed concentration as the reaction proceeds. Using the concept of mass balance which ensures mass conservation in a given volume (see, for example, [17, 18, 19] for mass conservation details), we obtain:

$$\mathbf{U} = \mathbf{U}_0 + \mathbf{U}_S + \mathbf{U}_T. \tag{7}$$

In a mass balance expression, transformed concentrations assume positive values if their corresponding species are reaction products and negative otherwise. If the extent of reaction is known, then the transformed concentration of a species can be quantified by the stoichiometric number and the extent of reaction [20]. This enables us to write mass balance expression for any species i, as follows [18]:

$$U_{r,i} = U_{0_{r,i}} + \sigma_{r,i}\ \chi_r + U_{S_{r,i}},\ i = 1, 2, \ldots, N_r,\ r = 1, \ldots, M \tag{8}$$

where $U_{0_{r,i}}, U_{S_{r,i}}$ are initial data and sources for the i^{th} species in the r^{th} reaction, and χ_r is the extent of reaction. If the species of interest corresponds to the n^{th} element in the subset $\mathbf{U}_r$, then its mass balance expression may be written as [18]:

$$\chi_r = -\frac{1}{\sigma_{r,n}}\Big(U_{0_{r,n}} + U_{S_{r,n}}\Big) + \frac{1}{\sigma_{r,n}}U_{r,n},\ n \in \{1, \ldots, N_r\}. \tag{9}$$

Substituting (9) into (8), we obtain [18]:

$$\begin{aligned} U_{r,i} &= U_{0_{r,i}} - \frac{\sigma_{r,i}}{\sigma_{r,n}}\Big(U_{0_{r,n}} + U_{S_{r,n}}\Big) + \frac{\sigma_{r,i}}{\sigma_{r,n}}U_{r,n} + U_{S_{r,i}}, \\ &= d_{r,i} + \frac{\sigma_{r,i}}{\sigma_{r,n}}U_{r,n},\ i = 1, \ldots, N_r,\ r = 1, \ldots, M,\ n \in \{1, \ldots, N_r\} \end{aligned} \tag{10}$$

where

$$d_{r,i} = U_{0_{r,i}} + U_{S_{r,i}} - \frac{\sigma_{r,i}}{\sigma_{r,n}}\Big(U_{0_{r,n}} + U_{S_{r,n}}\Big).$$

Using (10) in (5), a single-variable rate law for the r^{th} elementary reaction is obtained as follows:

$$R_r = K_{f,r}\prod_{i=1}^{N_{f,r}}\Big(d_{r,i} + \frac{\sigma_{r,i}}{\sigma_{r,n}}U_{r,n}\Big)^{\alpha_{r,i}} - K_{b,r}\prod_{j=1+N_{f,r}}^{N_{r,bf}}\Big(d_{r,j} + \frac{\sigma_{r,j}}{\sigma_{r,n}}U_{r,n}\Big)^{\alpha_{r,j}},\ r = 1, \ldots, M. \tag{11}$$

Moreover, let U_k in the global set $\mathbf{C}$ be the concentration of the species of interest that corresponds to the local concentration $U_{r,n}$ in reaction r. Then the source/sink term for the k^{th} species in the global set is given by [18]:

$$\begin{aligned} S_k &= \sum_{r=1}^{M}\sigma_{rn}R_r, \\ &= \sum_{r=1}^{M}\sigma_{rn}\Big(K_{f,r}\prod_{i=1}^{N_{f,r}}\Big(d_{r,i} + \frac{\sigma_{r,i}}{\sigma_{rn}}U_k\Big)^{\alpha_{r,i}} - K_{b,r}\prod_{j=1+N_{f,r}}^{N_r}\Big(d_{r,j} + \frac{\sigma_{r,j}}{\sigma_{rn}}U_k\Big)^{\alpha_{r,j}}\Big),\ k = 1, \ldots, N, \end{aligned} \tag{12}$$

where $\sigma_{r,n}$ is the stoichiometric coefficient of the species of interest in the r^{th} elementary reaction. Note that the source/sink term S_k defined by (12) is a polynomial in U_k only. Thus, using (12), Equation (3) can be independently (independent of other species transport equations) solved for the unknown U_k.

2.2. Acid drainage model

Due to different environmental and reaction conditions, effluent water composition varies from one system to another [13, 21, 22, 23, 24]. However there are some species

that are common to most of such systems. Following discussions in [25, 26, 27, 28, 29], the following set of species are common and will be considered in this discussion:

$$\mathbf{C} = \Big(H^+, Fe^{3+}, Fe^{2+}, Fe(OH)_3, SO_4^{2-}, Ca^{2+}, O_2, HCO_3^-\Big)$$

and the corresponding vector of concentrations is given by:

$$\mathbf{U} = \Big(U_1, U_2, U_3, U_4, U_5, U_6, U_7, U_8\Big).$$

Treatment implies neutralization of hydrogen ions, oxidation of ferrous ion and filtration of iron hydroxide concentration (with increasing time and distance). Following discussions in [31, 32], we employ a linear model for filtration of iron hydroxide which is a colloid. That is:

$$S_4 = -\theta_c \theta_L K_{dep,f} \mathcal{B} U_4, \tag{13}$$

where θ_L is specific surface area of the limestone, $K_{dep,f}$ is deposition rate constant, $\mathcal{B}$ is a dynamic blocking function and θ_c is a coupling parameter for measuring the surface area available for $Fe(OH)_3$ attachment at the limestone surfaces.

Following discussions in [33, 34] with a realistic assumption that the pH is less than 3.5, oxidation of ferrous ions follow:

$$Fe^{2+} + H^+ + 0.25O_2 \longrightarrow Fe^{3+} + 0.5H_2O. \tag{14}$$

at a rate given by:

$$S_3 = -\varepsilon_f K_o U_3 U_7, \tag{15}$$

where K_o includes Henry's constant. Note that ε_f appears in Equation (15) to indicate that the oxidation occurs in the void space (of the porous media) only.

Following the work of [33, 34, 36, 37], neutralization of hydrogen ions in the passive treatment is given by:

$$CaCO_3 + H^+ \rightleftharpoons Ca^{2+} + HCO_3^-. \tag{16}$$

which occurs at the following rate:

$$R_{CaCO_3} = -K_f\big((1-\theta_c)\mathcal{B}\big)\theta_L U_1 + K_b U_6 U_8 \tag{17}$$

Note that the surface area of the limestone available (after $Fe(OH)_3$ has been deposited) for hydrogen ion attachment and reaction is $\big((1-\theta_c)\mathcal{B}\big)\theta_L$. Using Equation (15) and (17), the net rate of neutralization of hydrogen ions is given by:

$$S_1 = -K_f\big((1-\theta_c)\mathcal{B}\big)\theta_L U_1 + K_b U_6 U_8 - \varepsilon_f K_o U_3 U_7. \tag{18}$$

By substituting Equations (13)-(18) in (3), a specific multi-scale linear model of the passive treatment method is given by:

$$\nabla \cdot \mathbf{v} = 0, \tag{19}$$

$$\varepsilon_f \nabla p = \varepsilon_f \rho \mathbf{g} - K_h \mathbf{v}, \tag{20}$$

$$\begin{aligned} \frac{\partial \varepsilon_f U_1}{\partial t} + \nabla \cdot \Big(\varepsilon_f \mathbf{v} U_1\Big) - \nabla \cdot \Big(\varepsilon_f \mathbf{D} \cdot \nabla U_1\Big) = \\ - K_f\big((1-\theta_c)\mathcal{B}\big)\theta_L U_1 + K_b U_6 U_8 - \varepsilon_f K_o U_3 U_7, \end{aligned} \tag{21}$$

$$\frac{\partial \varepsilon_f U_3}{\partial t} + \nabla \cdot \Big(\varepsilon_f \mathbf{v} U_3\Big) - \nabla \cdot \Big(\varepsilon_f \mathbf{D} \cdot \nabla U_3\Big) = -\varepsilon_f K_o U_3 U_7, \tag{22}$$

and

$$\frac{\partial \varepsilon_f U_4}{\partial t} + \nabla \cdot \Big(\varepsilon_f \mathbf{v} U_4\Big) - \nabla \cdot \Big(\varepsilon_f \mathbf{D} \cdot \nabla U_4\Big) = -\theta_c \theta_L K_{dep,f} \mathcal{B} U_4. \tag{23}$$

Observe in Equations (21) and (22), that current concentrations of calcium ions (U_6), hydrocarbonate ions (U_8) and oxygen (U_7) must be available for computations involving those equations. Thus the following three extra transport equations (that will account for the current concentrations of calcium ions, hydrocarbonate ions and oxygen) must be added to the system (19)-(23):

$$\frac{\partial \varepsilon_f U_6}{\partial t} + \nabla \cdot \Big(\varepsilon_f \mathbf{v} U_6\Big) - \nabla \cdot \Big(\varepsilon_f \mathbf{D} \cdot \nabla U_6\Big) = K_f\big((1-\theta_c)\mathcal{B}\big)\theta_L U_1 - K_b U_6 U_8, \tag{24}$$

$$\frac{\partial \varepsilon_f U_7}{\partial t} + \nabla \cdot \Big(\varepsilon_f \mathbf{v} U_7\Big) - \nabla \cdot \Big(\varepsilon_f \mathbf{D} \cdot \nabla U_7\Big) = -0.25 K_o U_3 U_7, \tag{25}$$

and

$$\frac{\partial \varepsilon_f U_8}{\partial t} + \nabla \cdot \Big(\varepsilon_f \mathbf{v} U_8\Big) - \nabla \cdot \Big(\varepsilon_f \mathbf{D} \cdot \nabla U_8\Big) = K_f\big((1-\theta_c)\mathcal{B}\big)\theta_L U_1 - K_b U_6 U_8. \tag{26}$$

Addition of the three transport equations (24)-(26) to the system (19)-(23) has resulted in a larger model with more degrees of freedom. This will increase the computational time of the model. A remedy is stoichiometric decoupling which is capable of reducing the system's degrees of freedom with a remarkable accuracy. Firstly, define the initial data of the species by the vector:

$$\mathbf{U}_0 = \Big(U_{10},\ U_{20}, \ldots, U_{80}\Big),$$

and assume that there are no sources or sinks (a closed reactor) so that the source/sink vector is given by:

$$\mathbf{U}_S = \Big(0,\ 0, \ldots, 0\Big).$$

There are two stoichiometric equations in the passive treatment process, thus $M = 2$. In the first equation (14) (i.e $r = 1$), we have the following data:

$$\begin{aligned} \mathbf{C}_1 &= \Big(Fe^{2+}, H^+, O_2, Fe^{3+}, H_2O\Big), \quad \alpha_1 = \Big(1, 0, 1, 0, 0\Big), \quad K_{b,1} = 0, \\ \sigma_1 &= \Big(-1, -1, -0.25, 1, 0.5\Big), \quad N_{f,1} = 2,\ N_1 = 5, \quad K_{f,1} = \varepsilon_f K_o. \end{aligned} \tag{27}$$

In the second equation (16) (i.e $r = 2$), we have the following data:

$$\begin{aligned} \mathbf{C}_2 &= \Big(CaCO_3, H^+, Ca^{2+}, HCO_3^-\Big), \quad \alpha_2 = \Big(0, 1, 1, 1\Big), \sigma_2 = \Big(-1, -1, 1, 1\Big) \\ N_{f,2} &= 2,\ N_2 = 4, \quad K_{f,2} = K_f\big((1-\theta_c)\mathcal{B}\big)\theta_L, \quad K_{b,2} = K_b. \end{aligned} \tag{28}$$

The first species is H^+ which corresponds to $k = 1$ in the global set $\mathbf{C}$, $n = 2$ in subset $\mathbf{C}_1$ and $n = 2$ in subset $n = 2$. Thus applying (27) and (28) in (12) and simplifying, we obtain:

$$S_1 = \alpha_{H1} C_1^2 + \alpha_{H2} C_1 + \alpha_{H3}, \tag{29}$$

where $\alpha_{H1} = -0.25\varepsilon_f K_o + K_b$, $\alpha_{H2} = -\varepsilon_f K_o\big(0.25C_{30} + C_{70} - 0.5C_{10}\big) - K_f\big((1-\theta_c)\mathcal{B}\big)\theta_L + K_b\Big(2C_{10} + C_{80} + C_{60}\Big)$ and $\alpha_{H3} = -\varepsilon_f K_o\big(C_{30} - C_{10}\big)\big(C_{70} - 0.25C_{10}\big) + K_b\Big(C_{10} + C_{80}\Big)\Big(C_{10} + C_{60}\Big)$.

The second species of interest is Fe^{2+} that corresponds to $k = 3$ in the global set $\mathbf{C}$ and $n = 1$ in the subset $\mathbf{C}_1$. Thus applying (27) in (12) and simplifying, we obtain:

$$S_3 = \alpha_{f1} C_3 + \alpha_{f2} C_3^2. \tag{30}$$

where $\alpha_{f1} = \varepsilon_f K_o\big(C_{70} + 0.25C_{30}\big)$ and $\alpha_{f2} = -0.25\varepsilon_f K_o$.

Thus, by closing the system (1)-(3) with (29) and (30) instead of in (15) and (18), a non-linear multi-scale model for the passive treatment method states that:

$$\nabla \cdot \mathbf{v} = 0, \tag{31}$$

$$\varepsilon_f \nabla p = \varepsilon_f \rho \mathbf{g} - K_h \mathbf{v}, \tag{32}$$

$$\frac{\partial \varepsilon_f C_1}{\partial t} + \nabla \cdot \Big(\varepsilon_f \mathbf{v} C_1\Big) - \nabla \cdot \Big(\varepsilon_f \mathbf{D} \cdot \nabla C_1\Big) = \alpha_{H1} C_1^2 + \alpha_{H2} C_1 + \alpha_{H3}, \tag{33}$$

$$\frac{\partial \varepsilon_f C_3}{\partial t} + \nabla \cdot \Big(\varepsilon_f \mathbf{v} C_3\Big) - \nabla \cdot \Big(\varepsilon_f \mathbf{D} \cdot \nabla C_3\Big) = \alpha_{f1} C_3 + \alpha_{f2} C_3^2, \tag{34}$$

and

$$\frac{\partial \varepsilon_f C_4}{\partial t} + \nabla \cdot \Big(\varepsilon_f \mathbf{v} C_4\Big) - \nabla \cdot \Big(\varepsilon_f \mathbf{D} \cdot \nabla C_4\Big) = -\theta_c \theta_L K_{dep,f} \mathcal{B} C_4, \tag{35}$$

2.3. Computational model

The rest of the discussion will involve a comparison to establish accuracy of the reduced model relative to the large model, thus we limit the rest of the discussion to one spatial dimension to enable a visual comparison. We consider a non-gravitational flow with velocity u units in the x direction for a distance of L_x units, in a time period T units. We further assume for simplicity, that the parameters in the model are constant and uniform throughout the domain. Thus, we set

$$\mathbf{v} = (u, 0, 0), \quad \nabla = \big(\frac{\partial}{\partial x}, 0, 0\big), \quad \mathbf{g} = (0, 0, g), \quad \text{and} \quad \mathbf{D} = \begin{bmatrix} \Gamma & 0 & 0 \\ 0 & 0 & 0 \\ 0 & 0 & 0 \end{bmatrix},$$

where Γ is the dispersion component in the x direction. Substituting into the non-linear model (Equations (31)-(35)) and linear model (Equations (19)-(26)) results in the initial-boundary value problem, find $\mathbf{U}(x,t)$ such that:

$$\frac{d}{dx} \rho \varepsilon_f u = 0, \tag{36}$$

$$u = -\frac{\varepsilon_f}{K_h} \frac{d}{dx} p \tag{37}$$

and

$$\frac{\partial \rho \varepsilon_f \mathbf{U}}{\partial t} + \frac{\partial}{\partial x}(\rho \varepsilon_f u \mathbf{U}) - \frac{\partial^2}{\partial x^2}(\Gamma \varepsilon_f \mathbf{U}) = \mathbf{S}_\mathbf{U}, \qquad \in [0, L_x] \times [0, T] \tag{38}$$

(note that $\rho = 1$ in the problem) subject to;

Inlet boundary	Initial conditions	Outlet boundary
$\mathbf{U}(0,t) = \mathbf{U}_{in}$	$\mathbf{U}(x, t=0) = \mathbf{U}_0$	$\frac{d}{dx}\mathbf{U}(L_x, t) = \mathbf{0}$

In the reduced non-linear model (Equations (31)-(35)), the vectors $\mathbf{U}, \mathbf{U}_{in}, \mathbf{U}_0,$ and $\mathbf{S_U}$ have three components each and are defined as follows;

$$\begin{aligned}
\mathbf{U} &= [C_1, C_3, C_4]^{\mathrm{Tr}},\\
\mathbf{U}_{in} &= [C_{10}, C_{30}, C_{40}]^{\mathrm{Tr}},\\
\mathbf{U}_0 &= [C_{10}, C_{30}, C_{40}]^{\mathrm{Tr}},\\
\mathbf{S_U} &= [\alpha_{H1}C_1^2 + \alpha_{H2}C_1 + \alpha_{H3}, \quad \alpha_{f1}C_3 + \alpha_{f2}C_3^2, \quad -\theta_c\theta_L K_{dep,f}\mathcal{B}C_4]^{\mathrm{Tr}},
\end{aligned}$$

where Tr means transpose.

In the original large linear model (Equations (19)-(26)), the vectors $\mathbf{U}, \mathbf{U}_{in}, \mathbf{U}_0,$ and $\mathbf{S_U}$ have six components each and are defined as follows;

$$\begin{aligned}
\mathbf{U} &= [C_1,\ C_3,\ C_4,\ C_6,\ C_7,\ C_8]^{\mathrm{Tr}},\\
\mathbf{U}_{in} &= [C_{10},\ C_{30},\ C_{40},\ C_{60},\ C_{70},\ C_{80}]^{\mathrm{Tr}},\\
\mathbf{U}_0 &= [C_{10},\ C_{30},\ C_{40},\ C_{60},\ C_{70},\ C_{80}]^{\mathrm{Tr}},\\
\mathbf{S_U} &= [-K_f\big((1-\theta_c)\mathcal{B}\big)\theta_L C_1 + K_b C_6 C_8 - \varepsilon_f K_o C_3 C_7, \quad -\varepsilon_f K_o C_3 C_7, \quad -\theta_c\theta_L K_{dep,f}\mathcal{B}C_4,\\
&\quad -\theta_c\theta_L K_{dep,f}\mathcal{B}C_4, \quad -0.25K_o C_3 C_7, \quad K_f\big((1-\theta_c)\mathcal{B}\big)\theta_L C_1 - K_b C_6 C_8]^{\mathrm{Tr}}.
\end{aligned}$$

3. Numerical modelling

In this section, a finite volume procedure (just to ensure that resulting schemes inherit the conservation property of the models in Section 2 above) is employed to discretize the spatial derivatives of the advection-diffusion-reaction equation and a time integration approach is employed to discretize the semi-discrete problem. The resulting numerical schemes will be used to simulate the multi-scale models developed in Section 2. The schemes presented here have been used by the authors in [38, 39] to successfully simulate physical problems. Our goal is to apply these standard schemes to the stoichiometric decoupling method, to investigate compatibility and suitability of the method for reactive transport problems.

3.1. Model discretization

We first discretize the spatial domain $[0, L_x]$ uniformly into N_x internal nodes such that $L_x = \Delta x \times N_x$, where Δx is the spatial step size. The nodes are placed in the domain such that the i^{th} internal node is located at $\frac{(2i-1)}{2}\Delta x$. Thus the tuple of discrete domain values is $[0, 0.5\Delta x, 1.5\Delta x, \ldots, L_x]$.

Next, we develop a control volume of length $\delta X_{we} = \Delta x$ with cross-sectional area A_c around each of the N_x nodes. The center of the control volume coincides with each internal node and its interfaces at boundary nodes coincide with the domain boundary interfaces. We denote current node by P, and its neighbours by $W = P-1$ for the western and $E = P+1$ for the eastern nodes, respectively. The western and eastern interfaces of the control volume are denoted by w and e, respectively (see Figures 1 and 2). The time interval $[0, T]$ is also discretized such that $\Delta t = \frac{T}{N_t}$, where Δt is the time step size and N_t is the total number of time steps.

We begin discretization of Equations (36)-(38) by integrating over the P^{th} control volume (which is defined by the spatial interval $[w, e]$ in Figure (2)) and also over the k^{th}

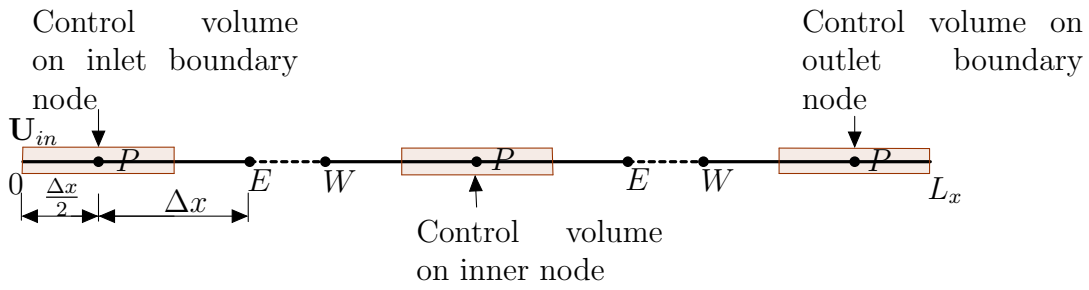

Figure 1: Domain discretization used in our discussion.

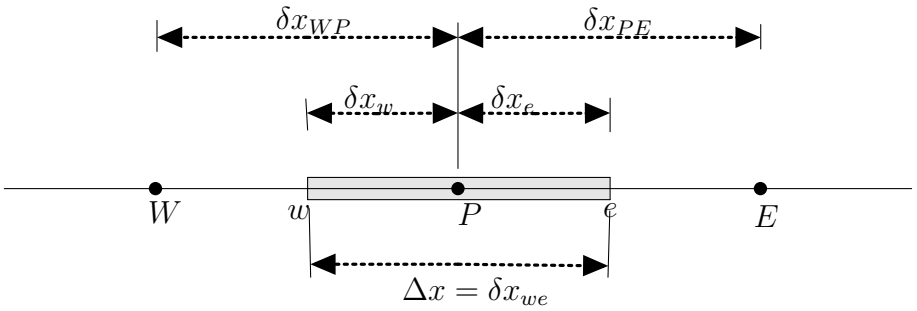

Figure 2: A control volume of an inner node P bounded to the west by node W and to the east by node E.

time interval $[t_k, t_{k+1}]$, as follows;

$$\int_{t_k}^{t_{k+1}} \int_w^e A_c \frac{d}{dx} \rho \varepsilon_f u dx dt = 0, \tag{39}$$

and

$$\int_{t_k}^{t_{k+1}}\int_w^e A_c\frac{\partial \rho\varepsilon_f U}{\partial t}dxdt + \int_{t_k}^{t_{k+1}}\int_w^e A_c\frac{\partial}{\partial x}(\rho\varepsilon_f uU)dxdt - \int_{t_k}^{t_{k+1}}\int_w^e A_c\frac{\partial^2}{\partial x^2}(\Gamma\varepsilon_f U)dxdt = \int_{t_k}^{t_{k+1}}\int_w^e A_c S_U dxdt. \tag{40}$$

Equation (39) becomes:

$$F_e - F_w = 0, \tag{41}$$

where $F_e = (\rho\varepsilon_f u A_c)_e$ and $F_w = (\rho\varepsilon_f u A_c)_w$ are the eastern and western convective fluxes across control volume interfaces. We linearize the source term (i.e. $S_U = b_0 - S_P U$, where S_P depends on previous values of U) and discretize the integrals in Equation (40) to obtain:

$$\begin{aligned} a_P^o(U_P^{k+1} - U_P^k) = &- (F_e U_e^{k+1} - F_w U_w^{k+1}) \\ &+ (A_c\Gamma\varepsilon_f)_e\Big(\frac{\partial U}{\partial x}\Big)_e^{k+1} - (A_c\Gamma\varepsilon_f)_w\Big(\frac{\partial U}{\partial x}\Big)_w^{k+1} \\ &+ \Delta x A_c b_0 - \Delta x A_c S_P U_P^{k+1}, \end{aligned} \tag{42}$$

where $a_P^o = \frac{\rho\varepsilon_f A_c \Delta x}{\Delta t}$. The notations U_e^{k+1}, U_w^{k+1} are values and $\left(\frac{\partial U}{\partial x}\right)_e^{k+1}, \left(\frac{\partial U}{\partial x}\right)_w^{k+1}$ are derivatives of U at time t_{k+1}, at the eastern and western interfaces of the control volume, respectively. The values U_e, U_w and derivatives $\left(\frac{\partial U}{\partial x}\right)_e, \left(\frac{\partial U}{\partial x}\right)_w$ do not fall on main nodes (*i.e.* P, E, W), thus are unknown. We approximate the derivatives using centred differencing as follows:

$$\Big(\frac{\partial U}{\partial x}\Big)_e^{k+1} \approx \frac{U_E^{k+1} - U_P^{k+1}}{\delta x_{PE}}, \quad \Big(\frac{\partial U}{\partial x}\Big)_w^{k+1} \approx \frac{U_P^{k+1} - U_W^{k+1}}{\delta x_{WP}}, \tag{43}$$

where $\delta x_{WP} = \delta x_{PE} = \Delta x$.

Substituting (43) into (42) we obtain;

$$\begin{aligned} a_P^o(U_P^{k+1} - U_P^k) = &- (F_e U_e^{k+1} - F_w U_w^{k+1}) \\ &+ D_e(U_E^{k+1} - U_P^{k+1}) - D_w(U_P^{k+1} - U_W^{k+1}) \\ &+ \Delta x A_c b_0 - \Delta x A_c S_P U_P^{k+1}, \end{aligned} \tag{44}$$

where $D_e = \frac{(A_c\Gamma\varepsilon_f)_e}{\delta x_{PE}}$ and $D_w = \frac{(A_c\Gamma\varepsilon_f)_w}{\delta x_{WP}}$ are diffusive fluxes across the eastern and western interfaces of the control volume. We now approximate the values U_e^{k+1} and U_w^{k+1} using the upwind differencing, central differencing and hybrid schemes of [38, 39].

3.2. Upwind differencing approximation

The upwind approximation for a positive flow direction where $F_e, F_w > 0$ is;

$$\begin{aligned} U_w^{k+1} &= U_W^{k+1} \\ U_e^{k+1} &= U_P^{k+1}. \end{aligned} \tag{45}$$

3.3. Central differencing approximation

The central differencing approximations of the values of U at the western and eastern interfaces are;

$$\begin{aligned} U_w^{k+1} &= \frac{1}{2}(U_W^{k+1} + U_P^{k+1}), \\ U_e^{k+1} &= \frac{1}{2}(U_P^{k+1} + U_E^{k+1}). \end{aligned} \tag{46}$$

3.4. Hybrid differencing approximation

We define the Peclet number at the control volume interfaces as;

$$P_e = \frac{F_e}{D_e} = \frac{F_w}{D_w}$$

The hybrid differencing scheme sets the diffusive fluxes in (44) to zero ($D_e = D_w = 0$) and substitutes the following piecewise expressions (based on Peclet number);

$$\begin{aligned} &U_w^{k+1} = \tfrac{1}{2}\big(1 + \tfrac{2D_w}{F_w}\big)U_W^{k+1} + \tfrac{1}{2}\big(1 - \tfrac{2D_w}{F_w}\big)U_P^{k+1} && \text{for } -2 < P_e < 2, \\ &U_w^{k+1} = U_W^{k+1}, \quad U_e^{k+1} = U_P^{k+1} && \text{for } P_e \geq 2, \\ &U_w^{k+1} = U_P^{k+1}, \quad U_e^{k+1} = U_E^{k+1} && \text{for } P_e \leq 2, \\ &U_e^{k+1} = \tfrac{1}{2}\big(1 + \tfrac{2D_e}{F_e}\big)U_P^{k+1} + \tfrac{1}{2}\big(1 - \tfrac{2D_e}{F_e}\big)U_E^{k+1} && \text{for } -2 < P_e < 2. \end{aligned}$$

3.5. Fully implicit schemes

In general, applying any of the schemes to approximate the unknown values in (44), will result in the linear system;

$$a_P U_P^{k+1} = a_P^o U_P^k + a_E U_E^{k+1} + a_W U_W^{k+1} + S_b, \tag{47}$$

where

$$
\begin{aligned}
a_P &= a_E + a_W + a_P^o - S_P, \\
F &= F_e = F_w = \rho \varepsilon_f u A_c, \\
D &= D_e = D_w = \frac{A_c \Gamma \varepsilon_f}{\Delta x}, \\
a_P^o &= \frac{\rho \varepsilon_f A_c \Delta x}{\Delta t}
\end{aligned}
$$

and the coefficients a_E, a_W, S_b are defined in Table 1 according to the scheme used.

Table 1: Coefficients for the algebraic model (47), according to spatial discretization schemes.

Differencing scheme	a_W	a_E	S_b
Upwind	$D + F$	D	$\Delta x A_c b_0$
Central	$D + \frac{F}{2}$	$D - \frac{F}{2}$	$\Delta x A_c b_0$
Hybrid	$\max\left(F, D + \frac{F}{2}, 0\right)$	$\max\left(-F, D - \frac{F}{2}, 0\right)$	$\Delta x A_c b_0$

Numerical scheme (47) is the standard Backward Euler time-integration scheme that has been coupled with either first order consistent Upwind or second order consistent Central differencing or Hybrid spatial discretizations (see a detailed discussion in [38, 39]). This standard Euler scheme is popular for its unconditional stability with respect to time-step size restrictions (i.e. unconditional stability with respect to the CFL condition). However, monotonicity properties ensure stability of numerical schemes when oscillations from the scheme are introduced by model parameters. Linear numerical schemes possess the monotonicity property if the posses diagonally-dominant coefficients and non-negative off-diagonal coefficients [40]. It is clear that scheme (47) possess the monotonicity property when the Upwind and Hybrid coefficients are used (see the coefficients in Table 1). Therefore, the Upwind and Hybrid schemes are unconditionally stable for all flow regimes. However the Central differencing coefficient a_E will fail to satisfy the monotonicity condition in a positive advection dominated flow case, i.e.

$$
a_E < 0, \quad \Longrightarrow \quad D - \frac{F}{2} < 0, \quad \Longrightarrow \quad P_e > 2.
$$

For practical applications where diffusive or dispersive transport is dominant (implying $P_e < 2$), the Central differencing coefficients will provide the best results (since it is second order consistent). For applications where there is a balance between advective or convective, and diffusive or dispersive transport, the Hybrid coefficients will provide the best results (since it is unconditionally stable and its order is between one and two). The Upwind coefficients will provide the efficient results in cases where advective or convective transport is dominant. In Section 4 below, we present numerical results to illustrate the

properties of scheme (47) under various flow regimes.

4. Numerical experiments

In this section, we present results obtained from numerical experiments involving the numerical schemes presented in Section 3 above. Results presented are on convergence tests for the schemes, accuracy test and simulation cost for the stoichiometric decoupling method presented in Section 2. The objectives are to show numerically, that the numerical schemes are convergent (thus are suitable for investigating the stoichiometric problem), to show that the stoichiometric decoupling method is accurate (thus can be applied to reactive transport problems) and finally, to show that the stoichiometric method can significantly reduce simulation cost. In Section 4.1, we present convergence results for the differencing schemes (i.e. only spatial discretizations, the Upwind, Central and Hybrid schemes). In Section 4.2, we present convergence results for the full schemes (both temporal and spatial discretizations). In Section 4.3, we presented accuracy results for the stoichiometric method discussed in Section 2. In Section 4.4, we present results on simulation cost for the stoichiometric method.

4.1. Convergence test: differencing schemes

In this section, we validate our experimental code and also assess the accuracy of the scheme (47), by comparing numerical solutions obtained with the Upwind, Central, and Hybrid coefficients with the analytical solution, for a steady one-dimensional scalar U transport. The analytical solution is [39]

$$U(x) = U_{in} + \frac{(U_{out} - U_{in}) \times \left(\exp(\frac{\rho u x}{\Gamma}) - 1 \right)}{\exp(\frac{\rho u L_x}{\Gamma}) - 1}, \tag{48}$$

where the parameters are given by;

$$L_x = 1\ m,\ \rho = 1\ Kgm^{-3},\ \Gamma = 0.1\ Kg(ms)^{-1},\ u = 0.1,\ U_{in} = 1\ Kg,\ U_{out} = 0.$$

Figure 3 shows that the numerical solution is accurate and that the accuracy increases as the number of grid points increase. Table 2 and Figure 4a show that the error between the analytical and numerical solution decreases monotonically as the grid gets finer, and therefore the Scheme 47 is convergent with the Upwind, Central differencing and Hybrid coefficients. However, while the Hybrid and Upwind coefficients make the scheme unconditionally stable, one can observe in Figure 4b that, the Central differencing coefficients make the scheme conditionally stable (i.e stable only when $|Pe| < 2$).

4.2. Convergence test: fully implicit schemes

Furthermore, we investigated the accuracy of the fully implicit scheme by comparing numerical solutions with the analytical solution for one-dimensional time-dependent diffusion of a scalar U, without sources or sinks, given by [39]:

$$U(x,t) = \frac{4U_0}{\pi} \sum_{n=1}^{\infty} \frac{(-1)^{n+1}}{2n-1} \exp(-\alpha_n \lambda_n^2 t) \cos(\lambda_n x), \tag{49}$$

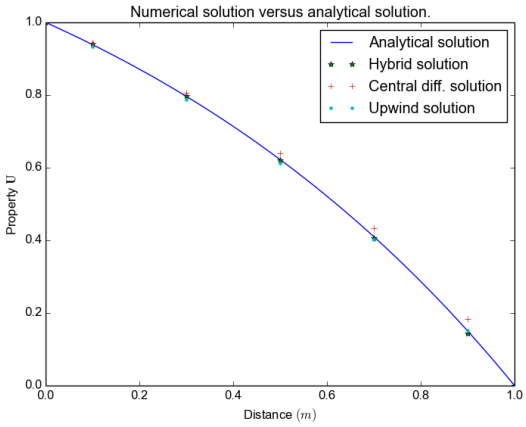

(a) Coarse grid (5 nodes).

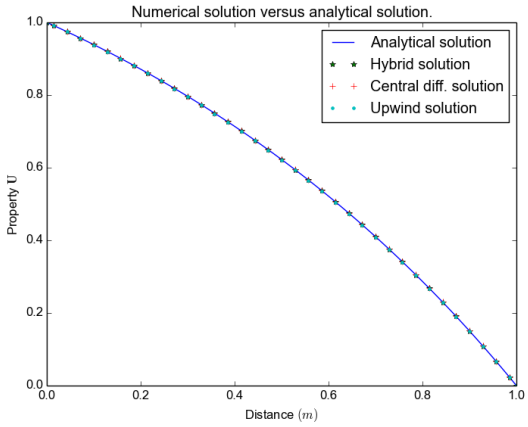

(b) Fine grid (35 nodes).

Figure 3: Solution of scheme (47) for 1 dimensional advection-diffusion equation, compared with its analytical solution (48).

Table 2: Errors of numerical scheme (47), according to Upwind, Central differencing and Hybrid coefficients and across grid spacing, with $\Gamma = 0.1, u = 0.1$.

Spatial schemes	$\max \lvert error \rvert, (\times 10^{-3})$			
	$N_x = 5$	$N_x = 10$	$N_x = 15$	$N_x = 20$
Upwind differencing	9.4562	5.2589	3.6581	2.8060
Central differencing	33.1232	8.1054	3.5741	2.0020
Hybrid differencing	6.1640	1.7484	0.8098	0.4650

where

$$\lambda_n = \frac{(2n-1)\pi}{2L_x}, \qquad \alpha_n = \frac{\Gamma}{\rho}, \tag{50}$$

$$L_x = 0.02\ m,\ \rho = 10^7\ Jm^{-3}K^{-1},\ \Gamma = 10\ W(mK)^{-1},\ u = 0.0\ ms^{-1},$$
$$U_0 = 200\ K,\ U_{out} = 0,\ \frac{\partial U}{\partial x}(0,t) = 0,\ T = 40\ s. \tag{51}$$

Figure 5 shows that the numerical solution is accurate and that the accuracy increases as the number of grid points increase. Table 3 and Figure 6 show that the error between the analytical and numerical solution decreases monotonically as the grid gets finer, thus the fully implicit scheme is a convergent scheme.

The summary in this section is that the schemes are accurate and convergent. The hybrid and upwind schemes are unconditionally stable while the central differencing scheme is stable when the Peclet numbers is low (more diffusion than advection). We can therefore, perform numerical experiments using a numerical code which is based on the fully implicit schemes.

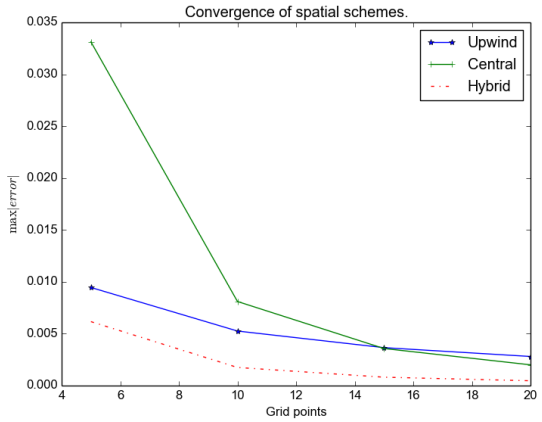

(a) Spatial error graphs.

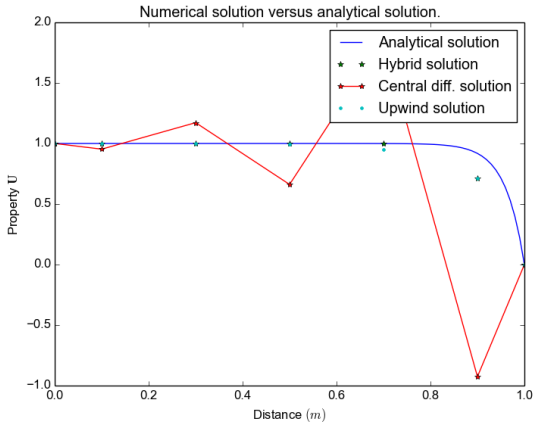

(b) Unstable central differencing scheme when $|P_e| > 2)$, $(u = 2.5,\ \Gamma = 0.1)$.

Figure 4: Convergence and stability according to the Upwind, Central differencing and Hybrid schemes.

Table 3: Errors of Scheme (47), according to the Upwind, Central differencing and Hybrid coefficients, and across grid spacing with $(\rho = 10^7, \Gamma = 10)$.

Grid points	Numerical scheme	max $\lvert error \rvert$			
		$N_t = 20$	$N_t = 40$	$N_t = 80$	$N_t = 120$
$N_x = 5$	Upwind differencing	6.6741	4.6611	3.6835	3.2026
	Central differencing	6.6741	4.6611	3.6835	3.2026
	Hybrid differencing	6.6741	4.6611	3.6835	3.2026
$N_x = 15$	Upwind differencing	4.0992	2.1609	1.2146	0.9026
	Central differencing	4.0992	2.1609	1.2146	0.9026
	Hybrid differencing	4.0992	2.1609	1.2146	0.9026
$N_x = 25$	Upwind differencing	3.9012	1.9727	1.0296	0.7185
	Central differencing	3.9012	1.9727	1.0296	0.7185
	Hybrid differencing	3.9012	1.9727	1.0296	0.7185

4.3. Accuracy test: Stoichiometric decoupling method

In this section, we present results of our numerical investigations on the reduction error between the stoichiometrically reduced model and the original large model. This error is defined as the difference of concentrations of species that are common (ferrous and hydrogen ions) to both models. However, from the results, the error defined by hydrogen was greater (worse) than the error defined by ferrous ions. Thus we choose to present and discuss the worse case only. The general input data for parameters in the models, that

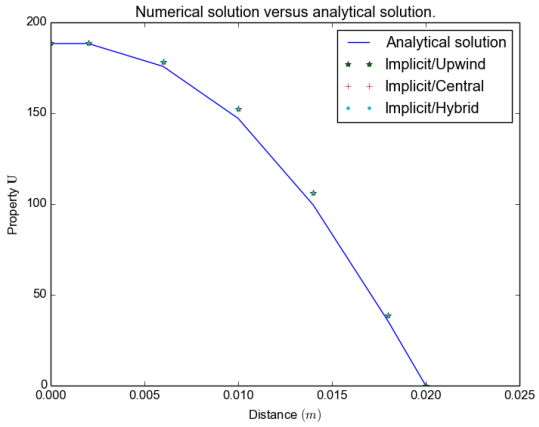

(a) Coarse grid (5×20).

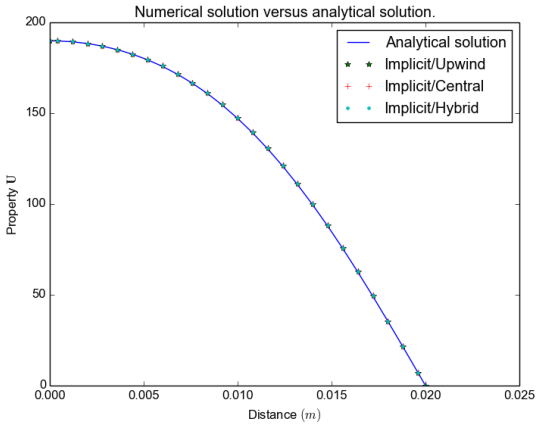

(b) Fine grid (25×160).

Figure 5: Solutions of one dimensional diffusion equation, obtained with Scheme (47) and compared with its analytical solution (49).

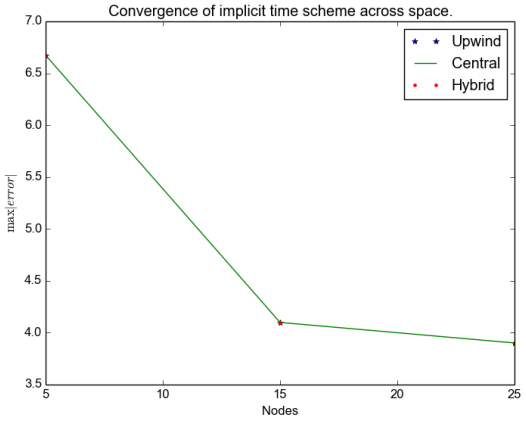

(a) Spatial errors.

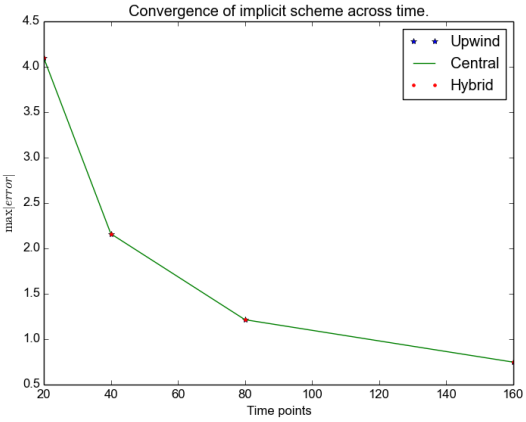

(b) Temporal errors.

Figure 6: Errors graphs of Scheme (47) Upwind, Central differencing and Hybrid schemes, and across grid spacing (step sizes).

we used in the experiments are given by:

$$L_x = 10,\ T = 50,\ \Gamma = 0.01,\ \rho = 1,\ \varepsilon_f = 0.1, \frac{d}{dx}p = 0.004,\ K_o = 0.025, \theta_c = 0.3,$$
$$\theta_l = 0.005,\ \beta = 0.001,\ K_f = 0.13,\ K_b = 0.0025,\ A_c = 1, K_h = 0.001, K_{dep,f} = 0.01,$$
$$C_{10} = 0.01,\ C_{30} = 0.0001, C_{40} = 0.02,\ C_{60} = 0.0001,\ C_{70} = 0.02, C_{80} = 0.0001.$$

The results show that the concentration of the contaminants in both reduced and large models, decrease with time and distance (see Figure 7), as expected in the passive treatment method. The worse case error between the reduced and large models is in the order 10^{-10}, which is remarkable. This error decreases with more time points and becomes stable with more spatial nodes (see Table 4).

Moreover, further investigations revealed that treatment occurs across different orders of magnitude of diffusion and advection (see Figures 8 and 9). The worse case error remains in the order 10^{-10} but varies across different orders of magnitudes of diffusities and velocities (see Tables 5 and 6).

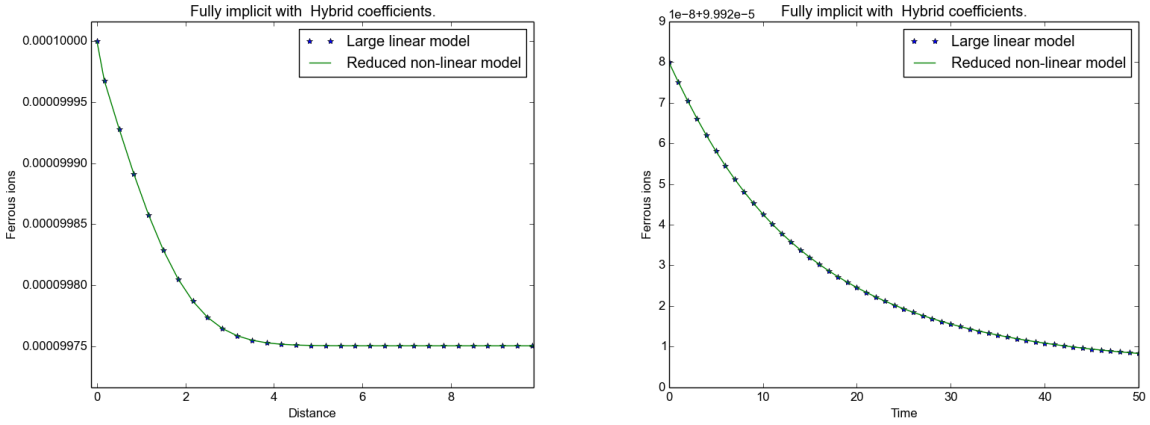

(a) Profile across space (30×50). (b) Profile across time (30×50).

Figure 7: Ferrous ion profiles in the large model (19)-(26) and reduced models (31)-(35) given in Section 2.2.

Table 4: Errors of the reduced non-linear model (31)-(35), across space, time and schemes with $\frac{d}{dx}p = -4 \times 10^{-10}, \Gamma = 0.1$.

Grid points	Numerical schemes	max $\lvert error \rvert$, $(\times 10^{-10})$			
		$N_t = 10$	$N_t = 20$	$N_t = 30$	$N_t = 50$
$N_x = 10$	Upwind differencing	4.2217	3.5411	3.5231	3.1327
	Central differencing	4.2215	3.5410	3.5230	3.1327
	Hybrid differencing	4.2217	3.5411	3.5231	3.1327
$N_x = 20$	Upwind differencing	4.2217	3.5411	3.5231	3.1327
	Central differencing	4.2216	3.5411	3.5231	3.1327
	Hybrid differencing	4.2217	3.5411	3.5231	3.1327
$N_x = 30$	Upwind differencing	4.2217	3.5411	3.5231	3.1327
	Central differencing	4.2217	3.5411	3.5231	3.1327
	Hybrid differencing	4.2217	3.5411	3.5231	3.1327

4.4. Simulation cost: Stoichiometric decoupling method

In this Section, we present and discuss results on cost of simulation for the models presented in Section 2. We measure cost by the CPU time, CPU time differences and relative CPU time that the numerical schemes require to solve the large linear model and the stoichiometrically reduced non-linear model. The CPU time differences and relative CPU time are defined as follows:

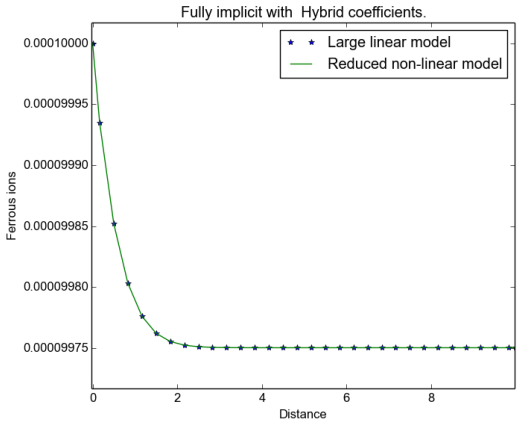

(a) Space, $\Gamma = 0.1$, $\frac{d}{dx}p = -4 \times 10^{-10}$.

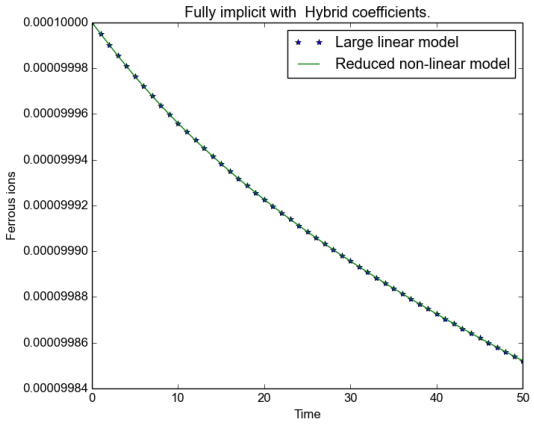

(b) Time, $\Gamma = 0.1$, $\frac{d}{dx}p = -4 \times 10^{-10}$.

Figure 8: Ferrous ion profiles in the large model (19)-(26) and reduced model (31)-(35), when diffusities and velocities are low.

Table 5: Errors of the reduced non-linear model (31)-(35), across space, time and schemes, with $\frac{d}{dx}p = -0.004, \Gamma = 0.01$. Note that $****$ means not applicable due to stability issues).

Grid points	Numerical schemes	$\max \lvert error \rvert, (\times 10^{-10})$			
		$N_t = 10$	$N_t = 20$	$N_t = 30$	$N_t = 50$
$N_x = 10$	Upwind differencing	4.2202	3.5408	3.5229	3.1326
	Central differencing	$****$	$****$	$****$	$****$
	Hybrid differencing	4.2206	3.5409	3.5230	3.1327
$N_x = 20$	Upwind differencing	4.2216	3.5411	3.5231	3.1327
	Central differencing	$****$	$****$	$****$	$****$
	Hybrid differencing	4.2217	3.5411	3.5231	3.1327
$N_x = 30$	Upwind differencing	4.2217	3.5411	3.5231	3.1327
	Central differencing	$****$	$****$	$****$	$****$
	Hybrid differencing	4.2217	3.5411	3.5231	3.1327

$$\text{CPU time difference} = \text{CPU}_L - \text{CPU}_S \tag{52}$$

and

$$\text{Relative CPU time} = \frac{\text{CPU}_L - \text{CPU}_S}{\text{CPU}_L} \tag{53}$$

where CPU_S is CPU time for the stoichiometrically reduced nonlinear model and CPU_L is CPU time for the original large linear model. In the experiments, we fixed the final time at ten ($T = 10$) and used a fine time resolution (5000 time steps) to ensure that results are not affected much by numerical discretization errors.

The final time was set at $T = 10$, *Upwind, Central and Hybrid* discretization were

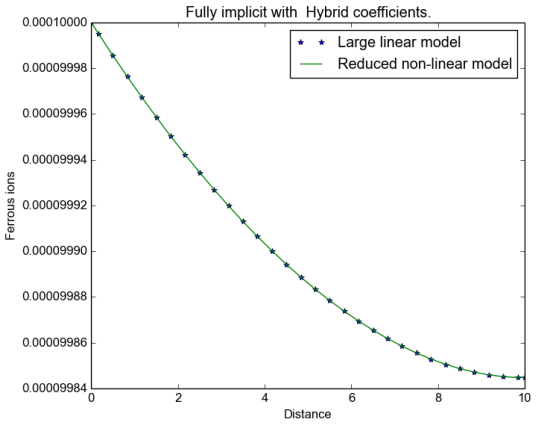

(a) Space, $\Gamma = 10$, $\frac{d}{dx}p = -0.008$.

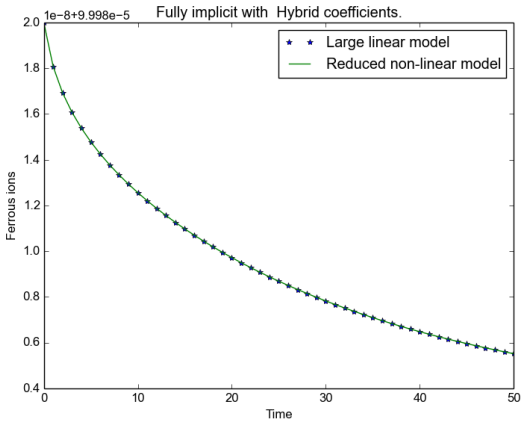

(b) Time, $\Gamma = 10$, $\frac{d}{dx}p = -0.008$.

Figure 9: Ferrous ion profiles in the large model (19)-(26) and reduced model (31)-(35), when diffusities and velocities are high.

Table 6: Errors of the reduced non-linear model (31)-(35) across diffusivities, pressure gradient and schemes, with $N_x = 30,\ N_t = 50$.

Dispersion	Numerical schemes	$\max\|error\|, (\times 10^{-10})$			
		$\frac{d}{dx}p = -4 \times 10^{-10}$	$\frac{d}{dx}p = -0.004$	$\frac{d}{dx}p = -0.006$	$\frac{d}{dx}p = -0.008$
$\Gamma = 0.1$	Upwind differencing	3.1327	3.1327	3.1327	3.1319
	Central differencing	3.1327	$****$	$****$	$****$
	Hybrid differencing	3.1327	3.1327	3.1327	3.1326
$\Gamma = 1$	Upwind differencing	3.1218	3.1030	3.0704	3.0157
	Central differencing	3.1154	$****$	$****$	$****$
	Hybrid differencing	3.1281	3.1087	3.0843	3.0423
$\Gamma = 10$	Upwind differencing	1.7284	1.5670	1.4876	1.4094
	Central differencing	1.7249	$****$	$****$	$****$
	Hybrid differencing	1.7284	1.5747	1.4985	1.4233

applied to both models presented in Section 2 and the CPU time for models were measured. Figures 10a, 10c and 10e show plots of CPU time against times steps. For all the schemes and for both models, the CPU time generally increased with increasing time steps, however, the CPU time for the stoichiometrically reduced nonlinear model recorded the least CPU time. Another observation is that, the CPU time difference between the stoichiometric model and the large linear model increased with increasing time steps. This observation can be seen clearly in Figures 10b, 10d and 10f.

Furthermore, to determine the CPU time saved by solving the stoichiometrically decoupled model instead of the large linear model, the CPU time differences for both models (measured across all discretizations) were normalized by the CPU time for the large model, (i.e using Equation (53)). Figure 11 shows the results of the investigation. About *80 percent* of CPU time will be saved if the stoichiometrically reduced nonlinear model is solved instead of the large linear model.

5. Conclusion

Mathematical models for reactive transport processes have high degrees of freedom due to the presence of many species, participating in large reaction mechanisms. Most often, not all the species profiles are of interest, but due to coupling with other species the entire set of equations in the model must be solved simultaneously. This is computationally expensive.

In this discussion, we have presented a model reduction procedure that is based on stoichiometry and mass balances. This procedure is capable of reducing the high degrees of freedom to any degree of interest (see Section 2.1 for details).

A multi-scale model with six degrees of freedom, that describes a passive treatment method for acidic mine effluents has been presented and reduced by the procedure to three degrees of freedom (follow the discussion in Section 2.2).

The resulting reduced model is non-linear, thus we presented numerical schemes that are based on finite volume and time integration dicretization procedures. Three spatial schemes (Upwind, Central differencing and Hybrid schemes) suitable for discretizing different flow-regime problems were coupled with backward Euler time approximation to obtain a fully implicit scheme for the time-dependent advection-diffusion-reaction Equation (follow the discussion in Section 3).

Numerical experiments were performed to verify the numerical schemes, and results show that the schemes were reasonably accurate and convergent (see Section 4.1 and 4.2). All the numerical schemes were applied to the large linear and reduced non-linear models (taking stability of the numerical schemes into consideration) in a numerical experiment, in order to establish accuracy of the Stoichiometric procedure (discussed in Section 2.1). The results showed that, the contaminant concentration (composed of ferrous ions, hydrogen ions and ferric hydroxide) in both reduced and large models, decreased in time and space as expected in the passive treatment method for mine effluent water. Furthermore, the results revealed a remarkable accuracy for the stoichiometric decoupling method even in the worse case. The reduction error did not cause stability issues for the numerical schemes (the numerical schemes were able to contain the reduction errors) for varying Peclet number conditions (follow the discussion in Section 4.3), this shows that the method is compatible with numerical schemes.

Moreover, experiments were performed to determine cost of simulation for both large linear and the stoichiometrically reduced nonlinear models using CPU time. Results showed that the stoichiometrically reduced model recorded the least CPU time, and the CPU time difference increased with increasing time steps. Relative CPU time difference showed that about *80 percent* of CPU time can be saved if stoichiometrically reduced nonlinear model is simulated instead of the original large linear model (follow the discussion in Section 4.4).

Therefore, we conclude based on the evidence provided that, the stoichiometric decoupling procedure is an efficient method for reducing simulation cost of reactive transport models, especially when some of the species are of interest as in this case of passive treatment of acidic mine effluent water.

Acknowledgement

AEA acknowledges support from the Pilot Bursary of the University of Pretoria, the African Institute of Mathematical Sciences and University of Stellenbosch. He is indebted to Prof. Franscois Smit for his invaluable advice.

References

[1] Ya-Jing H. and Wen-An Y., Partial equilibrium approximations in apoptosis I. The intracellular-signalling subsystem, Mathematical Biosciences 246, 27 -37 (2013).

[2] Ya-Jing H. and Wen-An Y., Partial equilibrium approximations in apoptosis II. The death-inducing signalling complex subsystems, Mathematical Biosciences 246, 27 - 37 (2013).

[3] S. Lam and D. Goussis, Understanding complex chemical kinetics with computational singular perturbation, in: Proceedings of International Symposium on Combustion Elsevier 22, 931 - 941 (1989).

[4] Goussis D. A., Quasi steady state and partial equilibrium approximations: their relation and their validity, Combustion Theory Model 16, 86 - 926 (2012).

[5] Huang Y. J., and Yong W. A., A stable simplification of a Fas-signaling pathway model for apoptosis, Proceedings of the 2012 IEEE 6th International Conference on Systems Biology (ISB), IEEE, 12 - 134 (2012).

[6] Keener J. P. and Sneyd J., Mathematical Physiology, Springer (1998).

[7] Djouad R. and Sportisse B., Solving reduced models in air pollution modelling, Applied Numerical Mathematics, 49 - 61 (2003).

[8] Fricker N., Beaudouin J., Richter P., Eils R., Krammer P.H., and Lavrik I.N., Model-based dissection of CD95 signaling dynamics reveals both a pro-and antiapoptotic role of c-FLIPL, Journal of Cell Biology 190, 377 - 389 (2010).

[9] Tobias S. R., Manuel A. C., Jose A. S., Carlos Ayora and Jesu Carrera, Field application of calcite Dispersed Alkaline Substrate (calcite-DAS) for passive treatment of acid mine drainage with high Al and metal concentrations, Applied Geochemistry 23, 1660 - 1674 (2008).

[10] Manuel A. C., Tobias S. R., and Veronica S., Implementation of an MgO-based metal removal step in the passive treatment system of Shilbottle, UK: Column experiments, Journal of Hazardous Materials 181, 92 - 930 (2010).

[11] Johnson D.B., and Hallberg K.B., Acid mine drainage remediation options a review, Science of the Total Environment 338, 3 - 14 (2005).

[12] Skousen. J. and Ziemkiewicz, P., Performance of 116 passive treatment systems for acid mine drainage, Proceedings of National Meeting of the American Society of Mining and Reclamation, Breckinridge, 110-1133 (2005).

[13] Alcolea A., Vazquez M., Caparros A., Ibarra I., Garcia C., Linares R. and Rodriguez, Heavy metal removal of intermittent acid mine drainage with an open limestone channel, Minerals Engineering 26, 86-98 (2012).

[14] Bear J. and Bachmat Y., A generalized theory on hydrodynamic dispersion in porous media, I. A. H. S. symposium, Artificial Recharge and Management of Aquifers, Haifer, Isreal P. N. 72, 7-16 (1967).

[15] Bachmat Y. and Bear J., Macroscopic modelling of transport phenomena in porous media 2: Application to Mass, Momentum and Energy transport, D. Reidel publishing company, 241-269 (1986) .

[16] Plessis J. P. and Masliyah J. H., Mathematical modelling of flow through consolidated isotropic porous media, Kluwer Academic publishers, 145-161 (1988).

[17] Formaggia L. and Scotti A., Positivity and conservation properties of some integration schemes for mass action kinetics, SIAM J. NUMER. ANAL. Vol 49, No. 3, (2011), pp 1267-1288

[18] Amikiya A.E. and Mapundi B., A stoichiometric method for reducing simulation cost of chemical kinetic models, Computers & Chemical Engineering 112 https://doi.org/10.1016/j.compchemeng.2018.02.020

[19] Walter J. Moore, Physical Chemistry, fifth edition, Prentice-Hall, Inc. (1972), ISBN 0-5824-44234-6

[20] Atkins P. W., Physical Chemistry, third edition, Oxford University Press (1987), ISBN 0-19-855196-7.

[21] Rimstidt J. D. and Vaughan D. J., Pyrite oxidation a state-of-the-art assessment of the reaction mechanism, Geochimica et Cosmochimica Acta 67, 873-880 (2003).

[22] Garrels R. M. and Thompson M. E., Oxidation of pyrite by iron sulphate solution, American Journal of Science 258, 57-67 (1960).

[23] Lowson R. T., Aqueous oxidation of pyrite by molecular oxygen, Journal of Chemical reviews 82, 461-497 (1982).

[24] Chandra A. P. and Gerson A. R., The mechanisms of pyrite oxidation and leaching: a fundamental perspective, Elsevier 65, 293-315 (2004).

[25] Smith E. E. and Shumate K. S., Water pollution control research series, U. S. Department of interior (1970).

[26] Bruno Bussiere, Acid mine drainage from abandoned mine site: Problematic and reclamation approaches, Proc. of Int. Symp. on Geoenvironmental Eng., ISGE2009, 8-10 (2009).

[27] Papirio S., Villa-Gomez D. K., Esposito G., Pirozzi F. and Lens P. N. L., Acid Mine Drainage Treatment in Fluidized-Bed Bioreactors by Sulfate-Reducing Bacteria: A Critical Review, Critical Reviews in Environmental Science and Technology 43, 254-2580 (2013).

[28] Sanchez-Andrea I., Sanz J. L., Martijn F. M. B., Alfons, and Stams J. M., Sulfate reduction at low pH to remediate acid mine drainage, Journal of Hazardous Materials 32(12), (2013).

[29] Richard T. A., David W. B., Brenda L. B., David C. S., Leslie S. and Ritchie A. I M., Waste-rock hydrogeology and geochemistry, Applied Geochemistry 57, 140-156 (2015).

[30] Gouin M., Saracusa E., Clemons C. B., Senko J., Kreider, K. L. and Young, G. W., A mathematical model of a passive scheme for acid mine drainage remediation, International Journal on Geomathematics 4, 27-53 (2013).

[31] Sun N. and Elimelech M. and Ne-Zheng S. and Ryan J. N., A novel two-dimensional model for colloid transport in physically and geochemically heterogeneous porous media, Contaminant Hydrology 49, 173-199 (2001).

[32] Mills W. B., Liu S. and Fong F. K., Literature Review and Model (COMET) for Colloid/Metal Transport in Porous Media, Ground Water 29, (1991).

[33] Werner S. and Lee F. G., Oxygenation of ferrous iron, American Chemical Society 53, 143-146 (1961).

[34] Ayora C., Manuel A. C., Francisco M., Tobias S. R., Jesus C. and Jose-Miguel N., Acid mine drainage in the Iberian Pyrite Belt: 2. Lessons learned from recent passive remediation experiences, Environ Sci Pollut Res, (2013). DOI10.1007/s11356-013-1479-2

[35] Williamson M. A. and Rimstidt J.D., The kinetics and electro-chemical rate determining step of aqueous pyrite oxidation, Geochimica et Cosmochimica Acta 58, 5443-5454 (1994).

[36] Plummer L. N. and Wigley T. M. and Parkhurst D. L., The kinetics of calcite dissolution in CO_2- water systems at 5^oC to 60^oC and 0.0 to 1.0 atm CO_2, American Journal of Science 278, 179-216 (1978).

[37] Reddy M. M. and Plummer L. N. and Busenberg E., Crystal growth of calcite from calcium bicarbonate solution at constant P_{CO_2} and 25^oC : a test of calcite dissolution model, Geochimica et Cosmochimica 45, 1281-1289 (1981).

[38] Patankar Suhas V. Series in computational methods in mechanics and thermal Sciences: Numerical Heat Transfer and Fluid Flow, Hemisphere Publishing Corporation (1980).

[39] Versteeg H. K. and Malalasekera W., An introduction to Computational fluid Dynamics: The finite Volume Method, Pearson Prentice Hall (2007).

[40] Eleuterio F. Toro, Riemann Solvers and Numerical Methods for Fluid Dynamics: A Practical Introduction (third edition), Springer-Verlag Berlin Heidelberg 2009 (ISBN 978-3-540-25202-3)

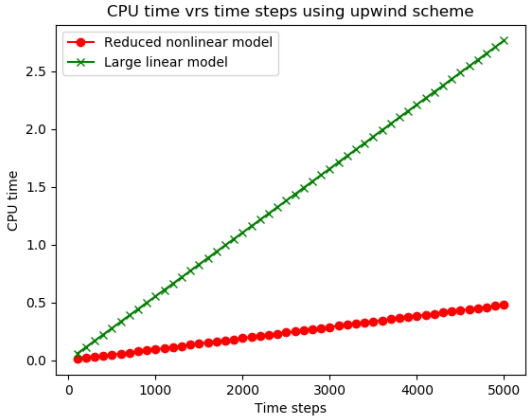

(a) CPU time using Upwind scheme.

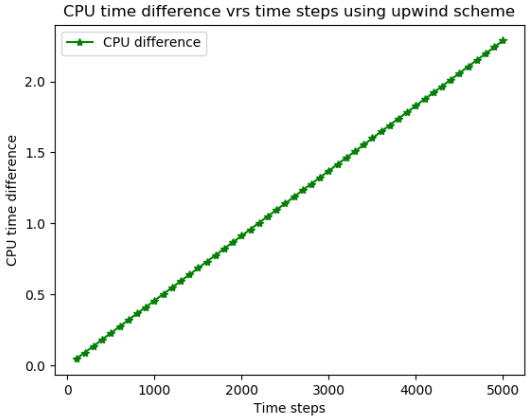

(b) CPU time difference using Upwind.

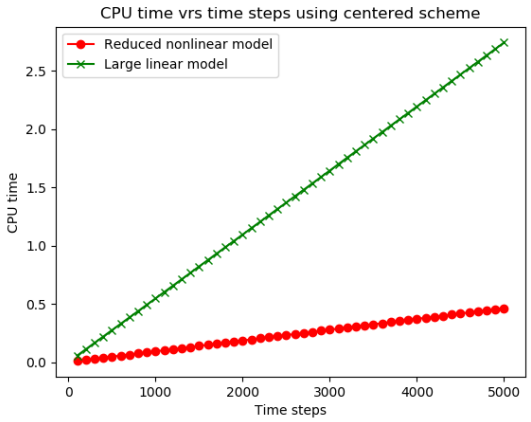

(c) CPU time using Central scheme.

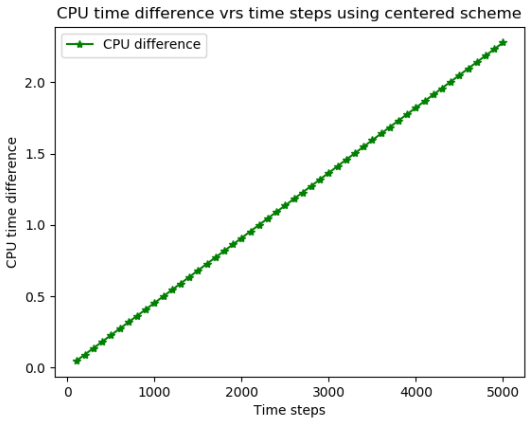

(d) CPU time difference using Central scheme

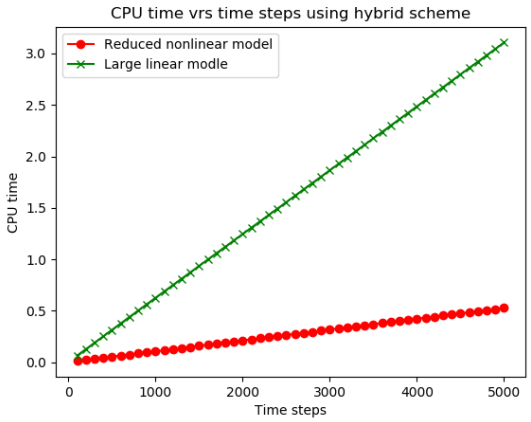

(e) CPU time using Hybrid scheme.

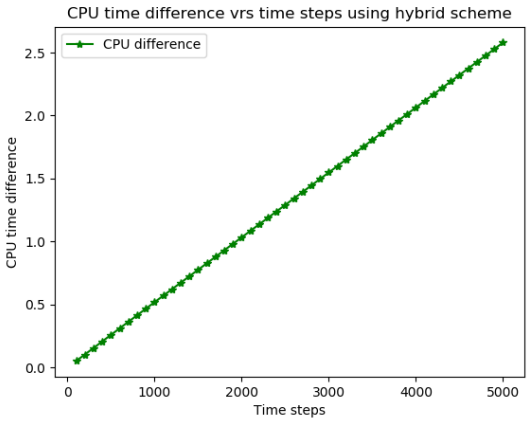

(f) CPU time difference using Hybrid scheme.

Figure 10: CPU time and CPU time differences for *large linear and reduced nonlinear models* using *Upwind, Central and Hybrid* schemes, measured across time steps using 10 spatial steps.

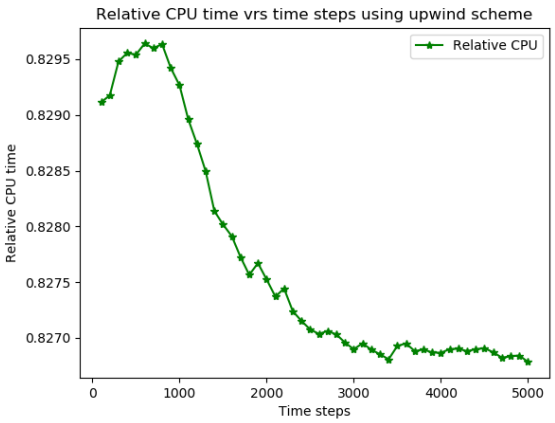

(a) Relative CPU time/Upwind/10 steps.

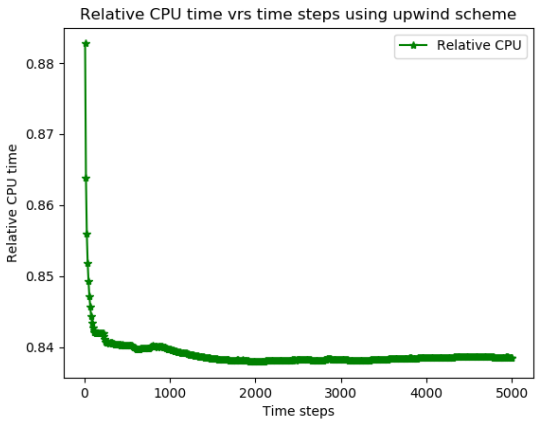

(b) Relative CPU time/Upwind/200 steps.

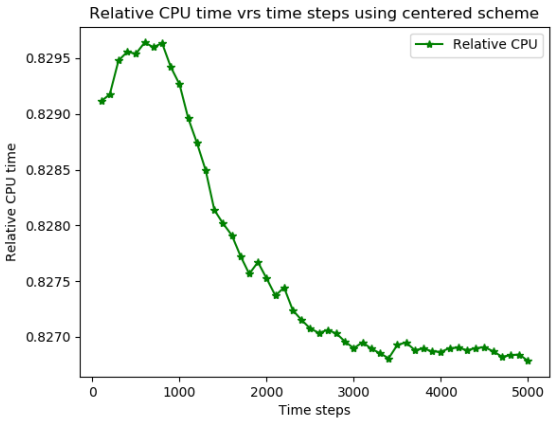

(c) Relative CPU time/Central/10 steps.

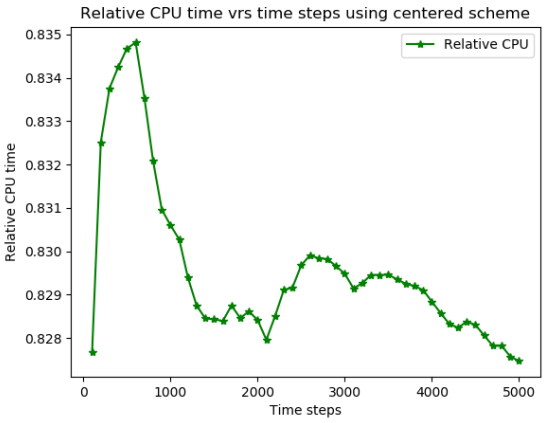

(d) Relative CPU time/Central/200 steps

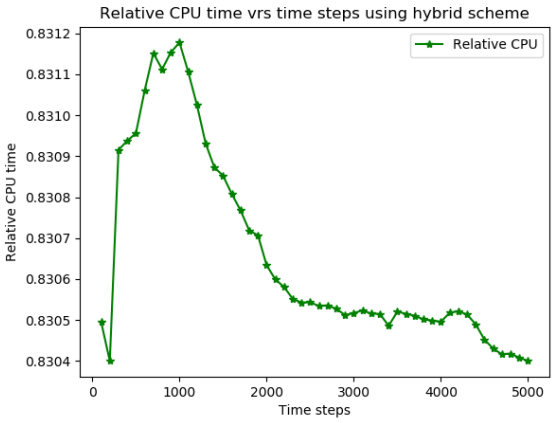

(e) Relative CPU time/Hybrid/10 steps.

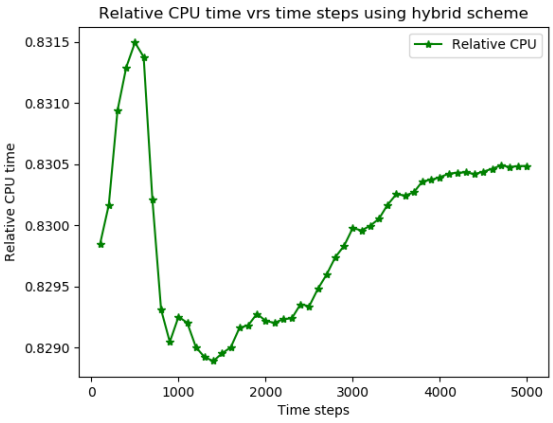

(f) Relative CPU time/Hybrid/200 steps.

Figure 11: Relative CPU time for the *large linear and reduced nonlinear models* using *Upwind, Central and Hybrid* schemes, measured across 5000 time steps using 10 and 200 spatial steps